Small

NANO · MICRO small
www.small-journal.com

RESEARCH ARTICLE

Vinylene-Bridge-Mediated Isomeric Dimer Acceptors With Ultranarrow-Bandgap for High-Sensitivity Near-Infrared Organic Photodetectors

Baofa Lan[1] | Yuyang Bai[1] | Wanying Feng[2] | Zhenhua Yang[3] | Yupu Wang[4] | Jia Wang[1] | Jingwen Yang[1] | Jiaying Wang[1] | Tianqi Chen[1] | Guankui Long[1] | Jian Zhu[3] | Miaomiao Li[4] | Bin Kan[1] | Yongsheng Chen[2]

[1]School of Materials Science and Engineering, National Institute for Advanced Materials, Nankai University, Tianjin, P. R. China | [2]State Key Laboratory and Institute of Elemento-Organic Chemistry, Frontiers Science Center For New Organic Matter, The Centre of Nanoscale Science and Technology and Key Laboratory of Functional Polymer Materials, Renewable Energy Conversion and Storage Center (RECAST), College of Chemistry, Nankai University, Tianjin, P. R. China | [3]School of Materials Science and Engineering, National Institute for Advanced Materials, Smart Sensing interdisciplinary Science Center, Nankai University, Tianjin, P. R. China | [4]School of Materials Science and Engineering, Tianjin Key Laboratory of Molecular Optoelectronic Science and Key Laboratory of Organic Integrated Circuits, Ministry of Education, Tianjin University, Tianjin, P. R. China

Correspondence: Bin Kan (kanbin04@nankai.edu.cn) | Yongsheng Chen (yschen99@nankai.edu.cn)

Received: 25 November 2025 | **Revised:** 4 February 2026 | **Accepted:** 6 February 2026

Keywords: dimer acceptor| isomeric strategy| multi-selenophene| narrow-bandgap acceptor| near-infrared organic photodetector

ABSTRACT

The development of dimeric acceptors (DMAs) for near-infrared optoelectronics is hindered by inherent structural limitations including compromised planarity and reduced conjugation, which lead to blue-shifted absorption spectra. Herein, we develop two vinylene-bridge-mediated isomeric DMAs based on multi-selenophene substitution, named DYSe-4 and DYSe-5, distinguished by the different spatial positions of vinylene bridges. The DYSe-4 and DYSe-5 demonstrate record-narrow optical band gaps of 1.29 and 1.27 eV. Compared to DYSe-4, DYSe-5 demonstrates reduced dihedral distortion, improved stacking orderliness, and enhanced intermolecular interaction. Consequently, the PBDB-T:DYSe-5-based rigid organic photodetector (OPD) achieves an ultralow dark current of 9.7×10^{-11} A cm^{-2} and a peak specific detectivity (D_{sh}*) of 9.7×10^{13} Jones at zero bias. The flexible counterpart exhibits a responsivity of 0.54 A W^{-1} at 870 nm, setting a new benchmark for flexible near-infrared OPDs. Extending beyond conventional externally powered photoplethysmography, we further construct a transmission-mode sensing platform by integrating a mechanoluminescence (ML) emitter with porcine skin tissue. This work not only achieves a further redshift in the absorption of DMAs and elucidates the structure-property-performance relationships of isomers but also establishes a foundational architecture for ML-driven health monitoring systems that operate without external power sources.

1 | Introduction

Near-infrared (NIR) light, known for its high atmospheric transmittance and superior tissue penetration, is pivotal to numerous military and civilian technologies such as night vision, remote sensing, and health monitoring [1–3]. In contrast to traditional inorganic semiconductors like silicon (Si) or indium gallium arsenide (InGaAs), organic NIR semiconductors present distinct benefits, including lightweight characteristics, intrinsic mechanical flexibility, and compatibility with large-area solution

Baofa Lan and Yuyang Bai contributed equally to this work.

processing. These attributes position them as a highly promising candidate for next-generation NIR devices, such as solar cells and photodetectors [4–7]. Nevertheless, the device performance of NIR organic semiconductors remains a critical bottleneck, largely due to the scarcity of high- performance electron acceptors that optimally balance a narrow optical bandgap with high photoelectrical responsivity and operational stability.

Recently, dimeric acceptors (DMAs) have emerged as a promising class of organic semiconductors that combine the batch reproducibility of small molecules and the superior stability of polymers. These merits make them highly attractive for developing efficient, stable, flexible and stretchable organic electronic devices [8–16]. Nonetheless, the structural planarity of DMAs is often compromised by the inherent dihedral angles between their monomeric units, resulting in a blue-shifted solid-state absorption that limits their utilization of NIR photons. To address this limitation, molecular design strategies focus on achieving a red-shifted absorption. A primary approach involves extending the conjugated backbone to narrow the optical bandgap. This can be effectively complemented by modifying side chains or terminal groups and incorporating heteroatoms [17, 18], all of which serve to enhance electronic interactions at either the intermolecular or intramolecular level [19–22]. Among these, replacing thiophene with selenophene stands out as a premier strategy for narrowing the bandgap, achieved by its dual ability to promote quinoid character and strengthen π-π stacking interactions. In our previous work, we developed a series of red-shifted dimeric acceptors (DYSe-1/2/3) via the selenophene substitution strategy and outer ring alkyl chain/terminal substitution (Figure S1) [23, 24], among which DYSe-3 achieved an optical bandgap of 1.35 eV with an absorption maximum at 842 nm, a milestone that represented the most red-shifted DMA reported at the time.

Despite this progress, achieving further red-shifting of the absorption spectra in DMAs continues to pose a considerable challenge, thereby limiting their broader application in various optoelectronic devices. The vinylene unit, composed of a σ-bond and a π-bond, effectively extends conjugation and redshifts absorption via highly delocalized π-electrons, which has been validated in the design of small-molecule acceptors and polymer acceptors [25–27]. Its non-distortable rigid structure further promotes molecular planarity and optimizes molecular packing. Therefore, the introduction of ethylene double bonds holds promise for further broadening the absorption range of dimers. More importantly, incorporating the vinylene bridge into DMA frameworks enables strategic isomer design through positional variation, offering a unique opportunity to elucidate structure-property relationships and guide the development of high-performance NIR dimers, a focused research direction that remains unexplored.

In this work, building upon prior multi-selenophene strategy, we further extended the absorption range of dimeric acceptors by incorporating vinylene bridges at distinct positions of the dimer backbone to enhance molecular conjugation, thereby designing and synthesizing two isomeric DMAs, DYSe-4 and DYSe-5. Both DMAs exhibit significantly redshifted absorption spectra spanning from 600 nm to 1000 nm. Particularly, the absorption maximum of DYSe-5 is determined to be 872 nm, which represents the most red-shifted value reported to date among all dimeric acceptors. Compared to DYSe-4, the additional ethylene double bonds in DYSe-5 are positioned closer to the central backbone of the dimer, extending the backbone conjugation length and thereby facilitating tighter π-π stacking. Theoretical calculation results reveal that DYSe-5 exhibits stronger acceptor-acceptor van der Waals interactions than DYSe-4 when blended with donor, thereby enabling more ordered intermolecular stacking. Among the evaluated devices, DYSe-5-based organic photodetector (OPD) achieves faster exciton dissociation and charge extraction rates, alongside a lower defect-state density, compared to DYSe-4 counterpart. Consequently, an optimal balance is achieved between a remarkable peak responsivity (R = 0.54 A W^{-1}) and a suppressed dark current (J_D = of 9.7 × 10^{-11} A cm^{-2}), coupled with a wide linear dynamic range (LDR) of 151 dB. The corresponding flexible device achieved a R of 0.54 A W^{-1} at 870 nm, representing the highest value reported so far for flexible photodetectors operating in the NIR-I spectral window (700–1000 nm), while also demonstrating excellent bending cycling stability. This work highlights the significant potential of central backbone conjugated extensions in developing high-performance near-infrared DMAs.

2 | Results and Discussion

The design strategy and structures of the dimers DYSe-4 and DYSe-5 are schematically illustrated in Figure 1a. As detailed in the Supporting Information, we synthesized these two DMAs through classic reactions such as Vilsmeier-Haack reaction, Stille coupling and Knoevenagel condensation. An additional vinylene bridge was introduced between the central core and the 1,1-dicyanomethylene-3-indanone (IC)/2-(6,7-difluoro-3-oxo-2,3-dihydro-1*H*-cyclopenta[b]naphthalen-1-ylidene)malon - onitrile (NIC) terminal groups. In DYSe-4, this vinylene bridge is situated on the IC/NIC side at the terminal end of the dimer. In contrast, in DYSe-5, the vinylene bridge is located on the IC/NIC side adjacent to the central backbone of the dimer. As a non-twisted and rigid linkage, the vinylene bridge is commonly employed to construct planar molecular frameworks. Furthermore, the introduction of the vinyl units can enhance the conjugation effect of the molecule, causing the absorption of the molecule to shift towards the NIR region. To investigate the influence of isomerization on the backbone planarity of DMAs, density functional theory (DFT) calculations were carried out at the B3LYP/6-31G level. As shown in Figure S2, both DMAs exhibited planar molecular conformations between the IC/NIC units and the thiophene linkers in their backbones. The average dihedral angles (θ_{avg}) for the two sides of the thiophene units were measured at 20.9° for DYSe-4 and 20.5° for DYSe-5. The smaller θ_{avg} value observed in DYSe-5 indicates a slight advantage in main-chain planarity, which facilitates more ordered intermolecular packing and enhancing electron mobility in thin films [10].

Molecular surface electrostatic potential (ESP) serves as a key indicator in judging intermolecular interactions and predicting electronic properties. The overall ESP distribution of DYSe-4 and DYSe-5 exhibits significant differences (Figure S3), the DMAs were divided into 15 fragments according to Figure S4, and their average ESP was calculated for each fragment. As shown in Figure 1b, the additional embedded vinylene double bond exerts

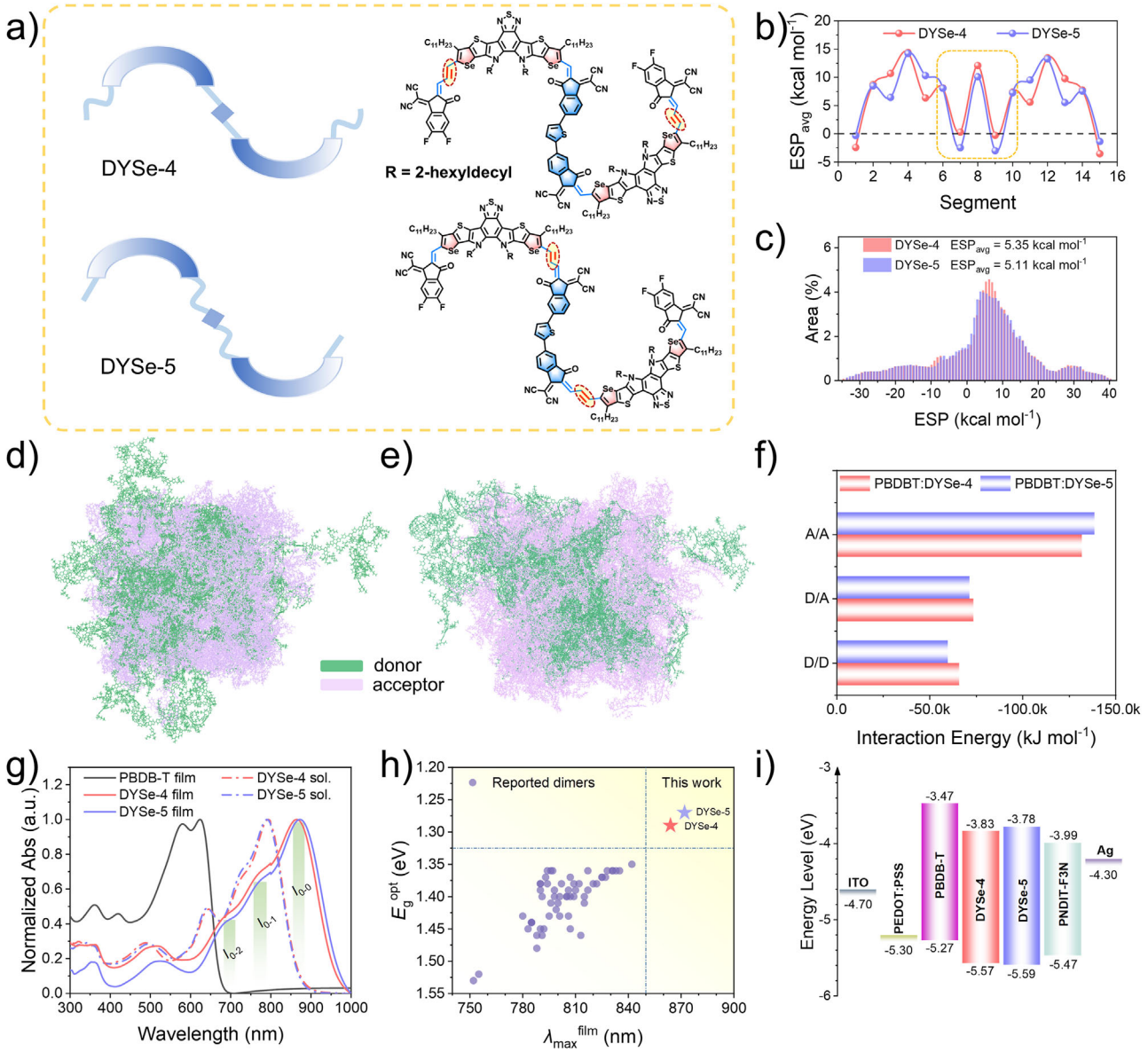

FIGURE 1 | (a) Molecular design strategy (left) and molecular structures (right) of DYSe-4 and DYSe-5. (b) ESP of fragments for DMAs. (c) The histograms of ESP area distribution of DMAs. MD simulation of the (d) PBDB-T:DYSe-4 and (e) PBDB-T:DYSe-5 blend films. (f) Statistical diagram of interaction energy in blend films. (g) Normalized UV-Vis-NIR absorption spectra for DMAs. (h) Summary of λ_{max}^{film} and E_g^{opt} of reported DMAs. (i) Energy level alignments of all materials in this work.

weak influence on the ESP of the linking unit itself but significantly alters the ESP of its adjacent groups. DYSe-5 exhibits fewer fragments with positive ESP values and lower corresponding values compared to DYSe-4, which can be primarily attributed to the pronounced negative electrostatic potential originating from the central IC/NIC segment in dimer DYSe-5. Besides, the area proportion of 5–10 kcal mol^{-1} decreases (Figure 1c) and the reduction in positive surface area corroborate the aforementioned phenomenon. On the other hand, the average ESP (ESP$_{avg}$) of DYSe-4 and DYSe-5 are 5.35 and 5.11 kcal mol^{-1}, respectively. Donor materials (such as PBDB-T) typically exhibit a relatively negative ESP distribution due to their high electron density. The smaller ESP difference between DYSe-5 and PBDB-T is thought to be beneficial for forming an optimized bulk heterojunction (BHJ) network [28–30]. To investigate the influence of different acceptors on the blend film formation kinetics, molecular dynamics (MD) simulations were performed on PBDB-T:DYSe-4 and PBDB-T:DYSe-5 blend films, as illustrated in Figure 1d, e, and detailed data are summarized in Table S1. The calculated donor/acceptor (D/A) interaction energy derived from Van der Waals forces for PBDB-T/DYSe-5 is lower than for PBDB-T/DYSe-4, corroborating the prior ESP results. Moreover, the stronger acceptor/acceptor intermolecular interaction observed among DYSe-5 compared to DYSe-4 suggests a potentially tighter A/A stacking in the PBDB-T:DYSe-5 blend film (Figure 1f), thereby facilitates the formation of long-range ordered charge transport pathways.

The photophysical behaviors of both DMAs and donor PBDB-T were investigated by ultraviolet-visible-near infrared (UV-vis-NIR) absorption spectroscopy. In dilute chloroform solution, the two acceptors exhibit nearly identical absorption profiles, featuring characteristic absorption maxima at 793 nm for

TABLE 1 | Optical properties of the dimers.

Molecule	$\lambda_{max}^{sol.}$ [nm]	λ_{max}^{film} [nm]	$\Delta\lambda_{film\text{-}sol.}$ [nm]	λ_{onset}^{film} [nm]	E_g^{opt} [eV][a]	E_{HOMO} [eV][b]	E_{LUMO} [eV][b]
DYSe-4	793	864	71	961	1.29	−5.57	−3.83
DYSe-5	790	872	82	976	1.27	−5.59	−3.78

[a]Calculated via thin film absorption onset ($E_g^{opt} = 1240/\lambda_{onset}^{film}$);
[b]Calculated via CV data.

DYSe-4 and 790 nm for DYSe-5, respectively (Figure 1g). Furthermore, both acceptors demonstrate unique absorption spectra characterized by triplet vibronic bands. As depicted in Figure S5, DYSe-5 exhibits a substantially higher *J* value (Ratio of 0-0 peak to 0–1 peak) compared to DYSe-4 (2.17 vs. 1.52), reveals a prevalence of *J*-aggregation behavior in DYSe-5 over DYSe-4 [31, 32]. It is noteworthy that the maximum film absorption peaks (λ_{max}^{film}) of DYSe-4 and DYSe-5 reach 864 nm and 872 nm (Table 1), which represent the most red-shifted DMAs reported to date (Table S2 and Figure 1h), with corresponding optical band gaps (E_g^{opt}) of 1.29 and 1.27 eV, respectively. The films of DYSe-4 and DYSe-5 exhibit redshifts of 71 nm and 82 nm, respectively, relative to their solution states. The larger redshift observed for DYSe-5 signifies superior molecular packing [33], as confirmed by grazing incidence wide-angle X-ray diffraction (GIWAXS) analysis showing a smaller π-π stacking distance and a larger coherence length (CL) (Figure S6 and Table S3). Figure 1i displays the energy level diagram derived from cyclic voltammetry determinations (Figure S7), the highest occupied molecular orbitals (HOMO)/lowest unoccupied molecular orbital (LUMO) energy levels for DYSe-4 and DYSe-5 are -5.57/-3.83 eV and -5.59/-3.78 eV respectively, exhibiting trends consistent with data obtained from DFT calculations (Figure S8). The slightly higher LUMO energy of the DYSe-5 helped in achieving a greater built-in electric field when blended with PBDB-T as a polymer donor, thereby more effectively driving the charge transport. It is worth noting that while the LUMO offset of PBDB-T:DYSe-5 (0.31 eV) is slightly smaller than that of PBDB-T:DYSe-4 (0.36 eV), it still exceeds the empirical threshold (≈ 0.3 eV) and remains sufficient to drive efficient exciton dissociation.

Subsequently, self-powered OPDs were fabricated with the structure of glass/ITO/PEDOT:PSS/PBDB-T:DYSe-4 (or DYSe-5)/PNDIT-F3N/Ag, and optimized details are shown in Tables S4, S5. The optimal donor-acceptor (D:A) weight ratios for the two systems were determined to be 1:1.4 and 1:1.5, respectively. While such discrepancies inevitably influence the morphology and optoelectronic properties of the blend films, this specific tailoring is essential to fully realize the maximum potential of each respective material combination. The dark current density (J_D), a critical parameter governing the detection limit of OPDs, was evaluated under zero bias conditions. The PBDB-T:DYSe-5-based device exhibited a notably lower J_D of 9.7×10^{-11} A cm^{-2}, approximately one-sixth that of the DYSe-4-based device (5.8×10^{-10} A cm^{-2}), as depicted in Figure 2a and Table 2. Spectral response measurements (Figure 2b) revealed a broad detection range of 300–1000 nm, with maximum *R* of 0.49 A W^{-1} and 0.54 A W^{-1} at NIR-I region for devices based on DYSe-4 and DYSe-5, respectively. As summarized in Figure 2c and Table S6, DYSe-4 and DYSe-5 demonstrate *R* values that rank among the highest achieved in self-powered NIR-OPDs. As presented in Figure 2d, the DYSe-4-based OPDs exhibited shot noise specific detectivity (D^*_{sh}) values above 10^{13} Jones across the 420–960 nm range, reaching a maximum of 3.6×10^{13} Jones at 860 nm. Owing to its superior responsivity and significantly suppressed dark current, the DYSe-5-based device achieved even higher D^*_{sh} values, exceeding 10^{13} Jones across the 380–960 nm spectral range and reaching a maximum of 9.7×10^{13} Jones, underscoring its enhanced broadband detection performance. Furthermore, based on the noise spectral density (S_n) at 5 Hz (Table 2), the calculated peak D^* reached 1.3×10^{12} Jones for the DYSe-4-based OPDs and 3.3×10^{12} Jones for the DYSe-5-based devices (Figure S9). Compared to DYSe-4, the DYSe-5-based device also exhibits faster photoresponse with a rise/fall time (t_{rise}/t_{fall}) of 5.4 µs/3.3 µs (Figure 2e), wider LDR of 151 dB (Figure 2f), and larger $f_{-3\,dB}$ of 85.2 kHz (Figure S10), indicating a promising future for applications with high LDR requirements, such as NIR imaging and health monitoring. The photoresponse time is also fast enough for high frame-rate video recording and optical communications [34]. Moreover, organic solar cell devices based on DYSe-5 also demonstrate superior performance compared to DYSe-4 devices, particularly in terms of short-circuit current density (Figure S11 and Table S7).

Apart from these, the impact of isomerization on exciton dissociation and charge collection in the devices was assessed via photocurrent density (J_{ph}) as a function of effective voltage (V_{eff}) [35]. In comparison with the PBDB-T:DYSe-5-based device (93%), the PBDB-T:DYSe-4-based organic photodetector exhibits a lower exciton dissociation efficiency (η_{diss}) of 91%. Furthermore, the former demonstrates a significantly higher charge collection efficiency (η_{coll}) of 77% compared to 65% for the latter, which serves as the dominant factor contributing to its superior sensitivity (Figure S12). The energetic disorder in the active layer can be quantified by the Urbach energy (E_U), obtained from the exponential tail in the Fourier-transform photocurrent spectroscopy EQE (FTPS-EQE) spectrum [36]. As shown in Figure 2g, devices with DYSe-5 exhibit a lower E_U of 22.7 meV compared to 25.3 meV for DYSe-4, indicating reduced disorder and narrower band-tail state distribution. Recent studies further link the thermal activation energy (E_a) of dark current to both the effective donor–acceptor energy offset (E_{eff}) and the density of band-tail states, emphasizing the significance of molecular design in noise suppression [37]. Since both devices utilize an identical donor, the shallower LUMO level of DYSe-5 creates a larger E_{eff} in its blend with PBDB-T relative to the DYSe-4-based counterpart. This synergistic effect between the increased E_{eff} and reduced E_U in the DYSe-5 device collectively contributes to a higher E_a, which in turn effectively suppresses the thermal generation of dark current [38].

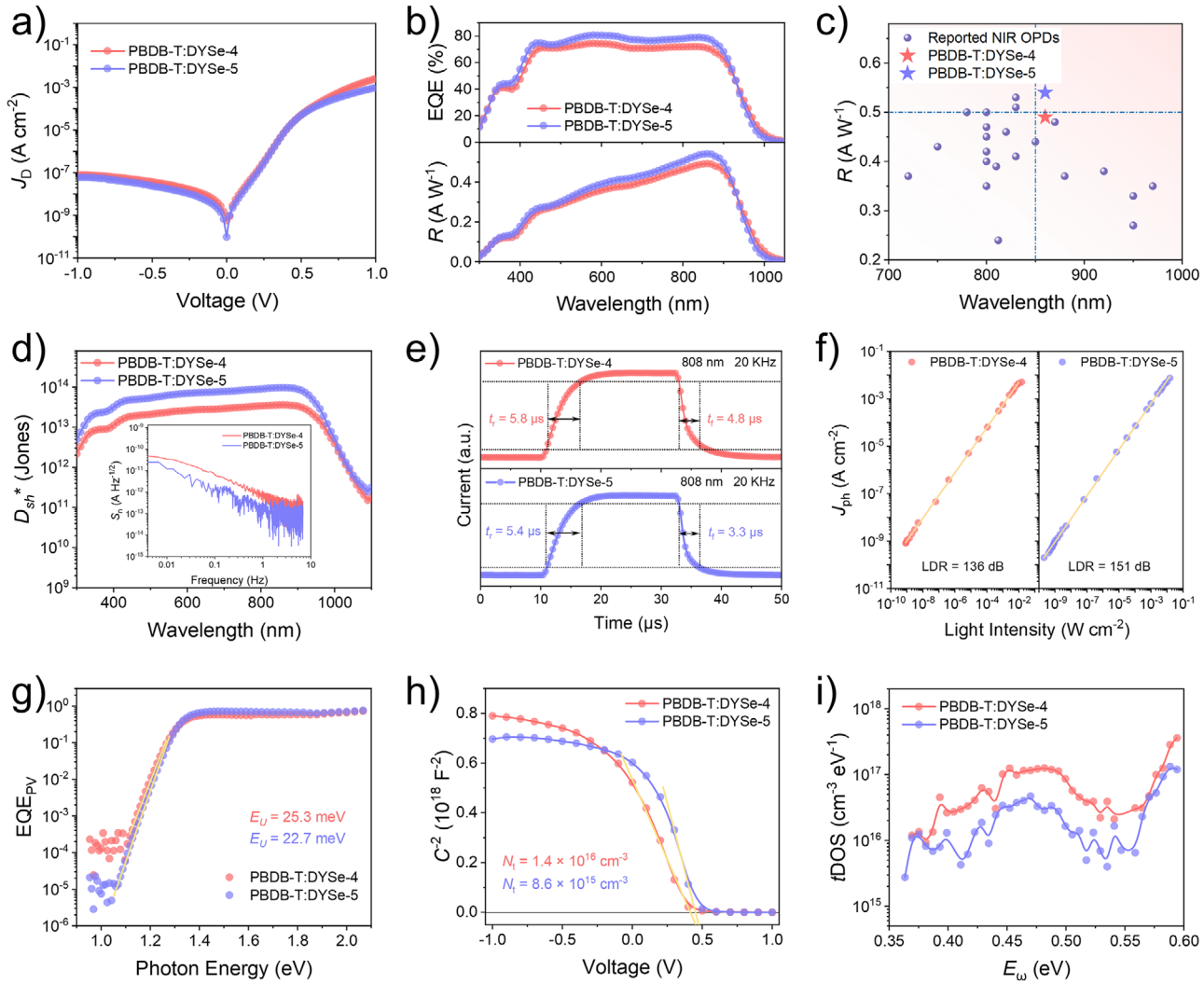

FIGURE 2 | (a) *J-V* curves of dimer-based OPDs under dark conditions. (b) EQE and *R* curves of dimer-based OPDs. (c) Summary of reported NIR-OPDs with high *R*. (d) The D_{sh}* curves of dimer-based OPDs, the inset is noise spectrum density. (e) Photoresponse time curves of the OPDs at 808 nm. (f) LDR of OPDs under the irradiation of 808 nm at zero bias. (g) FTPS-EQE curves of OPDs. (h) $1/C^2$-*V* curves of dimer-based OPDs and the Mott-Schottky linear fitting for them. (i) tDOS curves of OPDs.

TABLE 2 | Device performances of OPDs based on DYSe-4 and DYSe-5.

BHJ	J_D [A cm^{-2}][a]	R_{max} [A W^{-1}][a,c]	S_n [A Hz$^{-0.5}$][a,b]	$D_{sh,max}$* [Jones][a,c]
PBDB-T:DYSe-4	5.8×10^{-10}	0.49	1.9×10^{-13}	3.6×10^{13}
PBDB-T:DYSe-5	9.7×10^{-11}	0.54	8.2×10^{-14}	9.7×10^{13}

[a]Measured under 0 V;
[b]Abstracted under a frequency of 5 Hz;
[c]Abstracted at 860 nm.

Mott-Schottky analysis was performed to evaluate the trap density (N_t) of dimer-based OPDs (Figure 2h; Figures S13, S14) [39]. The PBDB-T:DYSe-5-based OPD exhibited a reduced N_t of 8.6×10^{15} cm^{-3} and an extended depletion width (W_D) of 132 nm, in contrast to the PBDB-T:DYSe-4-based device, which showed values of 1.4×10^{16} cm^{-3} and 98 nm, respectively. These characteristics are conducive to the suppression of dark current and promote effective dissociation of photogenerated excitons [33, 40]. To gain further insight into the distribution of trap density of states, capacitance-frequency (C-ω) measurements were conducted to probe the trap characteristics across varying energy depths. The resulting C-ω profiles and the corresponding density of trap states are presented in Figure 2i and Figure S15, respectively. Notably, within the shallow energy regime, the device incorporating DYSe-5 exhibits a markedly lower trap density compared to that based on DYSe-4, suggesting improved charge transport and collection efficiency. In contrast, both devices demonstrate comparable densities of trap states in the deeper energy

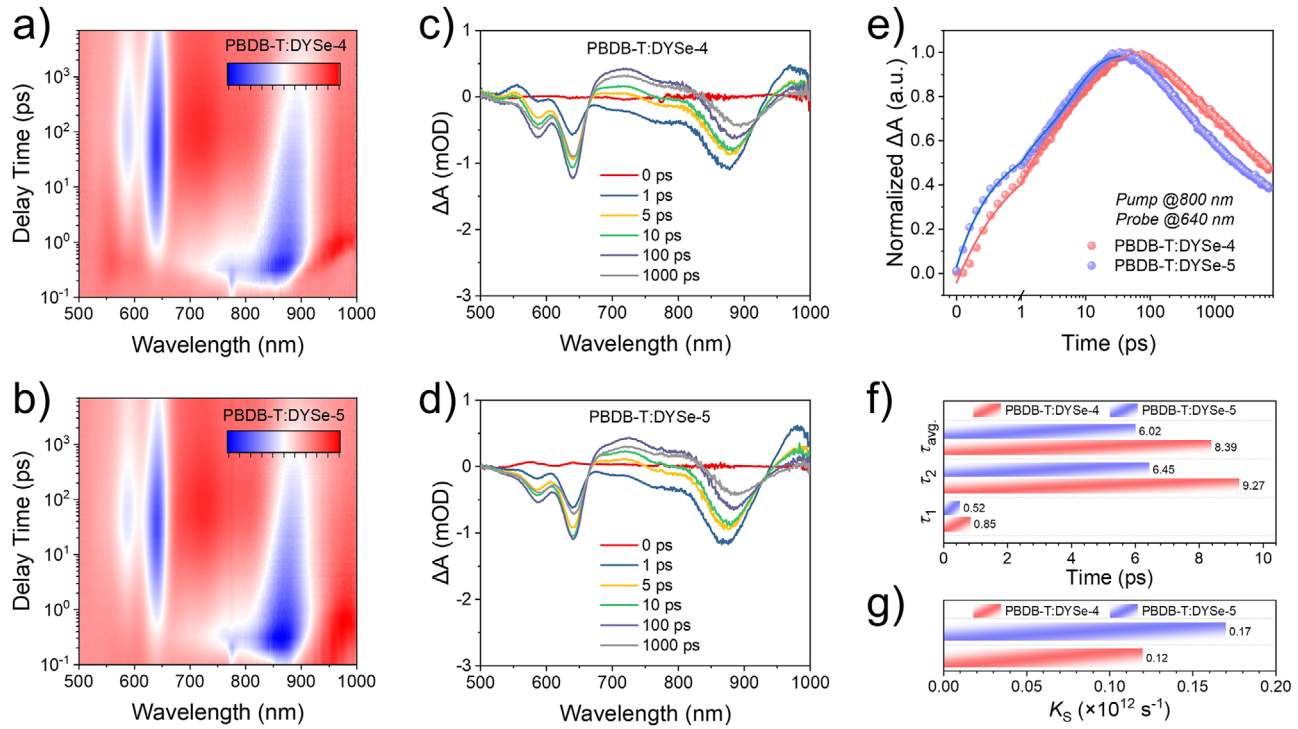

FIGURE 3 | (a, b) 2D fs-TAS images of blend films. (c, d) Time-resolved TAS of blend films under 800 nm pumping. (e) Dynamic curves and (f) detailed fitting parameters for the rise kinetics of blends probed at 640 nm. (g) The calculated results of K_S for blend films.

regions, implying similar nature and distribution of deep-level defects [38, 41].

Next, we employed femtosecond transient absorption spectroscopy (fs-TAS) to investigate the photo-induced charge transfer dynamics in dimer-based OPDs [42]. An 800 nm pump wavelength was specifically selected to resonantly excite the acceptor components at their characteristic absorption peak, thereby allowing the investigation of hole transfer dynamics within the corresponding blend films. Figure 3a, b present the 2D color plots of transient absorption for the blend films, while Figure 3c, d display the TA spectra of the three blend films at selected delay times. Ground state bleaching (GSB) features corresponding to the donor and acceptor appeared in the 530–670 nm and 810–950 nm spectral regions, respectively. Upon selective excitation of the acceptor, the GSB signal at 800 nm exhibited a rapid decay, concurrent with the growth of GSB signals at 584 nm and 640 nm, revealing efficient photoinduced hole transfer from DMAs to the PBDB-T. Additionally, a long-lived positive peak is present, which can be attributed to the absorption of the charge-separated state, indicating effective charge separation and stabilization [43]. The decay dynamics were further analyzed using a bi-exponential model: $I = A_1 \exp(-t/\tau_1) + A_2 \exp(-t/\tau_2)$, where τ_1 defines the time of exciton dissociation at the D/A interface, with τ_2 corresponding to the exciton diffusion within the acceptor domains [44]. By fitting the GSB signal at 640 nm (Figure 3e), we extracted the time constants for each blend film. For the PBDB-T:DYSe-5 blend, τ_1 and τ_2 were extracted as 0.52 and 6.45 ps, respectively (Figure 3f), notably shorter than the corresponding values for PBDB-T:DYSe-4 (τ_1 = 0.85 ps, τ_2 = 9.27 ps). These reduced time constants reflect accelerated dissociation and diffusion process of exciton within the PBDB-T:DYSe-5 blend, leading to suppressed exciton recombination while yielding enhanced responsivity and reduced dark current. The charge separation rate (K_S), defined as the inverse of the average carrier lifetime ($K_S = 1/\tau_{avg}$) [31], was derived from the fitting curves of 640 nm GSB signals. As summarized in Figure 3g and Table S8, the PBDB-T:DYSe-5 blend film exhibits a higher K_S value than PBDB-T:DYSe-4 blend film (0.17 vs. 0.12 × 10^{12} s^{-1}), further indicating more rapid charge separation in the PBDB-T:DYSe-5 system.

To investigate the evolution kinetics of blend films during thermal annealing, in situ absorption profiles for the PBDB-T:DYSe-4 and PBDB-T:DYSe-5 systems are provided in Figure 4a, b and Figure S16. The annealing process is generally characterized by three consecutive stages, initiating with heat transfer and residual solvent evaporation (stage I), followed by molecular reorganization (stage II), and culminating in the establishment of a final morphology (stage III) [45]. Both films were prepared with chloroform as the solvent and 1,8-diiodooctane as a processing additive. Owing to this formulation, stage I proceeded rapidly and was accompanied by minimal shift in the maximum absorption peaks. Nevertheless, a continuous reduction in absorption intensity was observed over time via in situ spectral mapping. This prompted a detailed analysis of the temporal evolution of the absorption intensity at 845 nm, corresponding to the characteristic wavelength of the acceptor materials. As shown in Figure 4c, stage II concludes more rapidly in the PBDB-T:DYSe-5 blend, with a duration of approximately 18.2 s, compared to 22.6 s for the PBDB-T:DYSe-4 blend. The shorter reorganization period of PBDB-T:DYSe-5 promotes faster crystallization, enabling the timely formation of a stable and favorable, ultimately supporting superior device performance [46].

The GIWAXS was employed to further elucidate the molecular packing of the blend films, as illustrated by the 2D diffraction

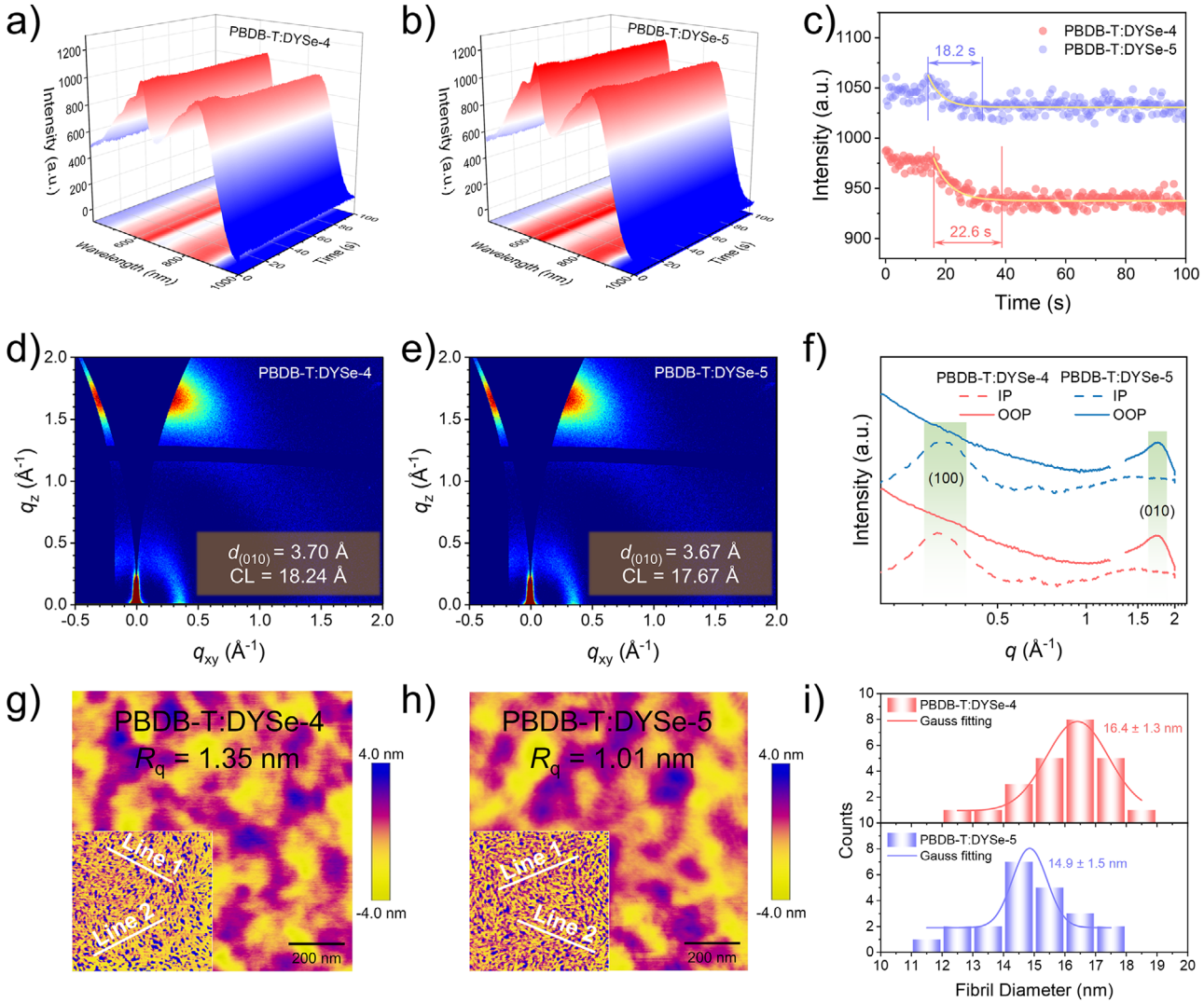

FIGURE 4 | (a, b) In situ thermal annealing absorption profiles of the dimer-based blend films. (c) Dynamic evolution of the peak intensity at 845 nm of DYSe-4 and DYSe-5 during thermal annealing. 2D GIWAXS images of (d) PBDB-T:DYSe-4 and (e) PBDB-T:DYSe-5 blend. (f) The line cut profiles of the dimer-based blend films. (g, h) AFM height and phase image of blend films. (i) Statistical particle size distribution diagrams of blend films.

maps and the corresponding line-cut profiles (Figure 4d, e), with quantitative parameters detailed in Table S3. Both blends display pronounced (010) diffraction signals along the out-of-plane (OOP) direction and (100) diffractions in the in-plane (IP) direction, indicating that the molecules adopt a predominantly face-on orientation [47]. Further evaluation of molecular ordering and crystallinity was performed based on the line-cut profiles of the (010) peaks in OOP direction (Figure 4f). In the PBDB-T:DYSe-4 and PBDB-T:DYSe-5 blends, the (010) diffraction peak were measured at 1.70 Å^{-1} and 1.71 Å^{-1}, respectively, and the corresponding *d*-spacing are 3.70 Å and 3.67 Å, which indicates a closer π-π stacking distance in the PBDB-T:DYSe-5 blend. Combine with the in situ absorption results, these observations suggest that the PBDB-T:DYSe-5 film forms a favorable nanoscale morphology through relatively rapid and controlled crystallization accompanied by tight π-π stacking, thereby facilitating improved charge transport and overall device performance. The surface topographies of the blend films were probed using atomic force microscopy (AFM), as illustrated in Figure 4g, h. Both the PBDB-T:DYSe-4 and PBDB-T:DYSe-5 blends manifest relatively uniform surfaces, yielding root-mean-square roughness (R_q) of 1.35 nm and 1.01 nm, respectively. Statistical analysis performed along the indicated directions (illustrations in Figure 4g, h) revealed a reduced fiber size of 14.9 nm for the PBDB-T:DYSe-5 blend, compared to 16.4 nm for PBDB-T:DYSe-4, as presented in Figure 4i and Figure S17. Such an optimized morphology for PBDB-T:DYSe-5, characterized by appropriate domain sizes, is highly conducive to efficient exciton dissociation, thereby mitigating charge recombination losses and augmenting charge transport capabilities. [48]

In addition to height/phase images, adhesion images (Figure 5a, b) were captured using AFM force spectroscopy, and the representative adhesion force spectroscopy images are shown in Figure 5c. The measured adhesion forces for PBDB-T:DYSe-4 and PBDB-T:DYSe-5 blend films were determined to be 33.6 nN and 46.1 nN, respectively. The significantly greater adhesion strength exhibited by the PBDB-T:DYSe-5 film promotes enhanced interfacial

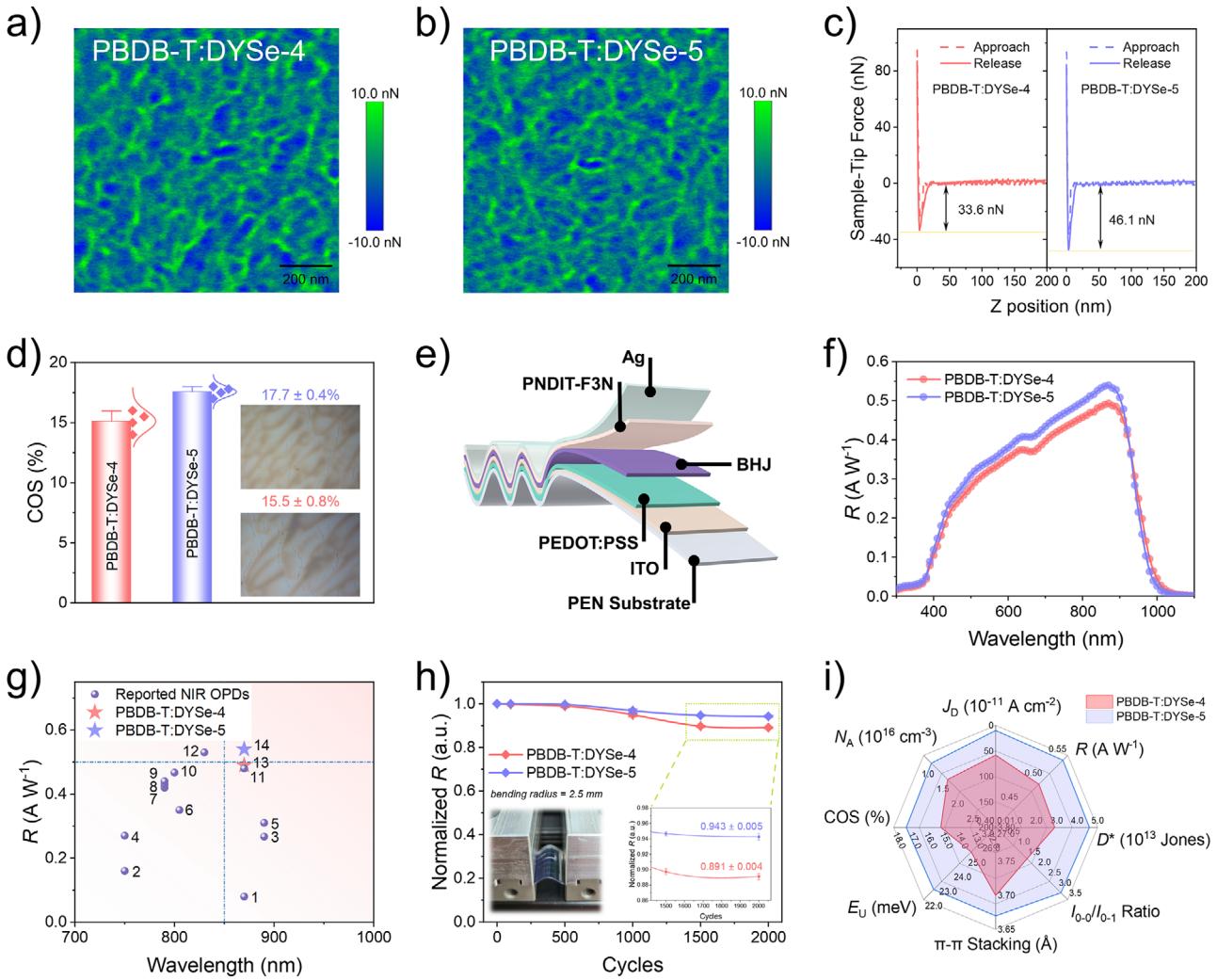

FIGURE 5 | AFM adhesion force mapping of (a) PBDB-T:DYSe-4 and (b) PBDB-T:DYSe-5. (c) AFM force spectroscopy for the tip interacting with different surfaces derived from the mappings. (d) Histograms of COS of the two blend films. The insets are optical micrographs of the formed cracks of PBDB-T:DYSe-4 and PBDB-T:DYSe-5 blend films by stretching on PDMS substrates. (e) Device structure of flexible OPDs. (f) *R* spectra of flexible OPDs. (g) Flexible NIR-OPDs with high *R* reported in the literature. (h) Normalized *R* of flexible OPDs versus bending cycles. (i) The radar chart to compare the molecular properties and device performance.

adhesion between the active layer and adjacent charge transport layers, which is expected to improved mechanical durability in flexible device [49]. Moreover, both blend films exhibit excellent crack onset strain (COS) of 15.5 ± 0.8% for PBDB-T:DYSe-4 and 17.7 ± 0.4% for PBDB-T:DYSe-5, as evaluated using a film-on-elastomer (FOE) method with polydimethylsiloxane as the compliant substrate (Figure 5d). These outstanding mechanical properties promote us to prepare flexible OPDs employing a PEN/ITO/PEDOT:PSS/BHJ/PNDIT-F3N/Ag architecture, as depicted in Figure 5e. Overall, the performance of flexible OPDs fabricated using both DMAs follows the same trend as that of rigid devices (Figure S18). It is worth noting that the device based on DYSe-5 achieved maximum *R* values of 0.54 A W^{-1} at 870 nm (Figure 5f), which presents the highest responsivity among all flexible OPDs operating in the NIR-I region, as demonstrated in Figure 5g and Table S9. The mechanical stability of OPDs was further evaluated through cyclic bending tests at a radius of 2.5 mm (Figure 5h). After 2000 bending cycles, the device based on DYSe-5 retained 0.943 ± 0.005 of its initial responsivity, significantly outperforming its DYSe-4 counterpart, which retained only 0.891 ± 0.004. These mechanical performance trends align well with the AFM adhesion force and crack onset strain measurements. Furthermore, a comparison of the performance retention from rigid to flexible devices was conducted for both dimers. As shown in Table S10, the flexible device based on DYSe-5 retains 42% of the detectivity achieved by its rigid counterpart, outperforming the 33% retention rate observed for the DYSe-4-based flexible device. The superior performance of flexible DYSe-5 devices originates from the extended conjugation and tighter molecular packing, which not only ensure high initial responsivity but also enhance mechanical stability through better stress distribution.

Integrating experimental characterizations with theoretical analysis elucidates the critical role of the connecting moiety in governing the performance of dimer-based organic photodetectors. This structure-property relationship is quantitatively visualized via the radar chart in Figure 5i. Relative to the shorter linkage in DYSe-4, the extended connecting group via a vinylene double bonds

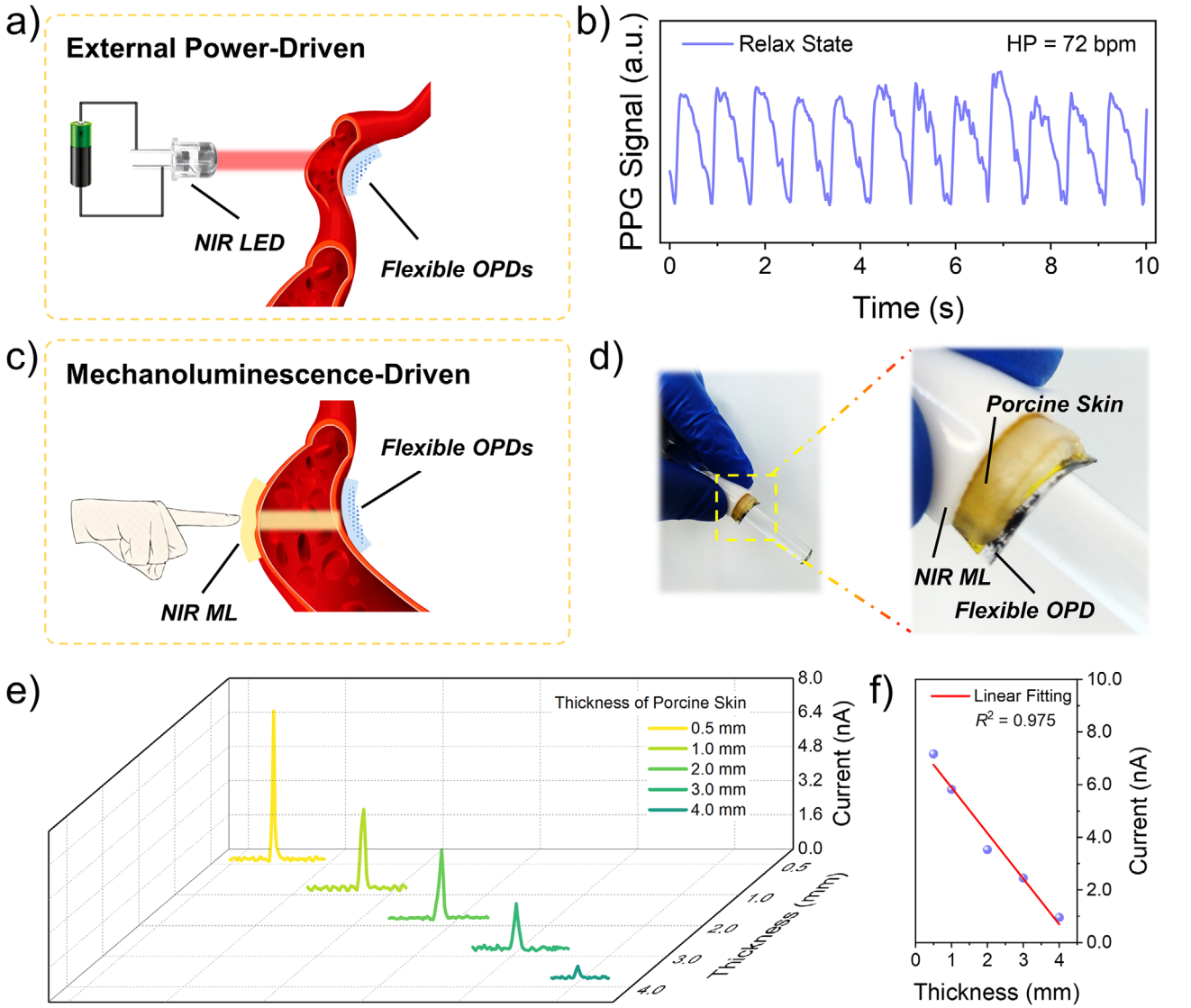

FIGURE 6 | (a) Schematic diagram for heart rate monitoring under traditional external power driven, and (b) PPG signals detected by DYSe-5 based OPD at 808 nm. (c) Schematic diagram for healthy monitoring under ML driven. (d) Actual photograph of the ML/porcine skin/flexible OPD laminated structure. (e) Current-time curves obtained from ML/porcine skin/ flexible OPD system testing at different porcine skin thicknesses and (f) corresponding linear fitting of current and porcine skin thickness.

in DYSe-5 promotes tighter intermolecular packing, a higher propensity for *J*-aggregation, diminished structural disorder, and an increased crack onset strain. Overall, these advantageous characteristics, coupled with the selenophene substitution at the central core, operate synergistically to enhance both the optoelectronic performance in NIR region and mechanical durability of PBDB-T:DYSe-5-based OPDs.

Building on this demonstration of favorable responsivity and mechanical stability in dimer-based OPDs, a flexible PBDB-T:DYSe-5 based OPD was fabricated and attached to a fingertip to function as a photoplethysmography (PPG) sensor (Figure 6a) [50]. As shown in Figure 6b, a heart rate of 72 bpm was recorded from the subject in a relax state using the flexible OPD, indicating a representative heart rate in the acceptable range for an adult aged 15–30. Building upon the low dark current/high sensitivity flexible OPD, we now developed a mechanoluminescence (ML)-driven transdermal sensing platform that eliminates the need for external power sources and active light illumination. This integrated system consists of three key components: a red-emitting $Gd_3Ga_5O_{12}:Eu^{3+}$/PDMS ML patch as a stress-activated light source (triggered by human motions such as finger pressing or thoracic expansion during breathing) [51], porcine skin tissue phantoms (simulating human skin with thicknesses ranging from 0.5 to 4.0 mm, matching the optical refractive index (1.37–1.41) of human skin) as the target tissue [52], and the DYSe-5-based flexible OPD as the signal detector (Figure 6c, d). Figure S19 displayed the emission spectrum and mechanical cycling stability of the ML patch. A fixed mechanical pressure was applied to the ML layer to trigger stable red-light emission, which penetrated the porcine skin (Figure S20) and was subsequently detected by the flexible OPD (Figure 6e). The resulting photocurrent signals exhibited a strong linear dependence on the porcine skin thickness (Figure 6f), with a correlation coefficient (R^2) of 0.975, which is sufficient to distinguish between normal skin (0.5–1.0 mm), subcutaneous fat accumulation (>2.0 mm), and

mild edema (a 0.3 mm+ increase in skin thickness, a key indicator of inflammation or tissue damage). This integrated approach not only validates the novel marriage of OPD and ML technologies but also pioneers a route towards passive-driven health monitoring, which are anticipated in handheld wearable medical devices and postoperative stress monitoring for artificial joint replacements [53]. The practical deployment of ML-OPD PPG sensors not only requires flexible OPDs with low noise and high sensitivity, but also necessitates the development of ML materials featuring low excitation thresholds and long emission lifetimes.

3 | Conclusions

In summary, this work developed two ultranarrow-bandgap dimeric electron acceptors by employing a synergistic approach involving multi-selenophene substitution and isomeric strategy. This deliberate isomerization modulates molecular conformation and ESP distribution, with DYSe-5 exhibiting enhanced backbone planarity, predominant *J*-aggregation behavior, and optimized molecular packing. DYSe-5 exhibits a lower average ESP than DYSe-4, particularly across the central backbone. This reduction leads to a smaller ESP difference with the donor PBDB-T, favoring moderate donor-acceptor intermolecular interactions that suppress both geminate and non-radiative recombination pathways, resulting in improved the charge generation efficiency. Utilizing these advantages, a notably low dark current of 9.7×10^{-11} A cm^{-2} and an outstanding D_{sh}* of 9.7×10^{13} Jones (at 860 nm) were achieved in the rigid PBDB-T:DYSe-5 device. Furthermore, the flexible OPD utilizing DYSe-5 demonstrates a peak responsivity of 0.54 A W^{-1}, marking the optimal metric reported so far for flexible NIR-OPDs. The practicality of the flexible PBDB-T:DYSe-5 OPD is successfully validated through health monitoring applications, encompassing both conventional external power-driven PPG and a newly proposed mechanoluminescence-driven transdermal sensing platform. This study highlights the crucial role of vinylene-bridge-mediated isomerization in advancing high-performance NIR dimer acceptors, provides fundamental insights into structure-property relationships, and demonstrates the promising integration of low-noise/high-sensitivity NIR-OPDs with stress-activated ML systems for passive health monitoring.

Acknowledgements

The authors gratefully acknowledge the financial support from the Ministry of Science and Technology of the People's Republic of China (2023YFE0210400), National Natural Science Foundation of China (U25A20572, 22361132530, 52573199, and 52303237), Natural Science Foundation of Tianjin (24JCYBJC01540), and the Fundamental Research Funds for the Central Universities of Nankai University (023-63253172, 020–63251184).

Conflicts of Interest

The authors declare no conflict of interest.

Data Availability Statement

The data that support the findings of this study are available from the corresponding author upon reasonable request.

References

1. Y. Li, X. He, S. C. Chen, and N. Zhao, "Intelligent Photodetectors: Post-manufacturing Tunability toward Enhanced Performance and Advanced Functions," *Chemical Reviews* 125 (2025): 6977–7022, https://doi.org/10.1021/acs.chemrev.4c00763.

2. K. Zhang, J. Wu, C. Sun, D. S. Chung, Y. Geng, and L. Ye, "The Rising Promise of Organic Photodetectors in Emerging Technologies," *Nature Reviews Materials* 10 (2025): 487–489, https://doi.org/10.1038/s41578-025-00821-2.

3. Y. Ding, S. Xiong, L. Sun, et al., "Metal Nanowire-based Transparent Electrode for Flexible and Stretchable Optoelectronic Devices," *Chemical Society Reviews* 53 (2024): 7784–7827, https://doi.org/10.1039/D4CS00080C.

4. W. Song, Q. Ye, Z. Chen, J. Ge, L. Xie, and Z. Ge, "Advances in Stretchable Organic Photovoltaics: Flexible Transparent Electrodes and Deformable Active Layer Design," *Advanced Materials* 36 (2024): 2311170, https://doi.org/10.1002/adma.202311170.

5. H. Chen, Y. Cai, Y. Han, et al., "Towards Artificial Visual Sensory System: Organic Optoelectronic Synaptic Materials and Devices," *Angewandte Chemie International Edition* 63 (2024): e202313634, https://doi.org/10.1002/anie.202313634.

6. C. Geng, G. Song, W. Lin, et al., "Flexible photonic contactless human-machine interface based on visible-blind near-infrared organic photodetectors," *National Science Review* 12 (2025): nwaf303, https://doi.org/10.1093/nsr/nwaf303.

7. X. Zhao, H. Qu, Z. Zhuo, et al., "Highly Sensitive Near-Infrared Narrowband Photomultiplication Type Organic Photodetectors via Employing Charge Injection Narrowing and Exciton Dissociation Narrowing Strategy," *Advanced Functional Materials* (2025): 22181, https://doi.org/10.1002/adfm.202522181.

8. J. Wang, P. Wang, T. Chen, et al., "Isomerism Effect of 3D Dimeric Acceptors for Non-Halogenated Solvent-Processed Organic Solar Cells with 20 % Efficiency," *Angewandte Chemie International Edition* 64 (2025): 202423562, https://doi.org/10.1002/anie.202423562.

9. Y. Ding, W. A. Memon, S. Xiong, et al., "Molecular Design of Dimeric Acceptor Enables Binary Organic Solar Cells with 19.78% Efficiency and Enhanced Stability," *Advanced Materials* 37 (2025): 2501671, https://doi.org/10.1002/adma.202501671.

10. Y. Li, Z. Ge, L. Mei, et al., "Isomeric Dimer Acceptors for Stable Organic Solar Cells with over 19 % Efficiency," *Angewandte Chemie International Edition* 63 (2024): 202411044, https://doi.org/10.1002/anie.202411044.

11. B. Fan, H. Gao, L. Yu, et al., "Local Structure-Induced Selective Interactions Enables High-Performance and Burn-in-Free Organic Photovoltaics," *Angewandte Chemie International Edition* 64 (2024): 202418439, https://doi.org/10.1002/anie.202418439.

12. H. Lai, Y. Zhu, C. Shan, et al., "Decoding Molecular Conformations of Dimeric Non-Fullerene Acceptors for High-Sensitivity Near-Infrared Organic Photodetectors," *Angewandte Chemie International Edition* 64 (2025): 19630, https://doi.org/10.1002/anie.202519630.

13. S. Li, R. Zhang, M. Zhang, et al., "Tethered Small-Molecule Acceptors Simultaneously Enhance the Efficiency and Stability of Polymer Solar Cells," *Advanced Materials* 35 (2022): 2206563, https://doi.org/10.1002/adma.202206563.

14. H. Wang, C. Cao, H. Chen, et al., "Oligomeric Acceptor: a "Two-in-One" Strategy to Bridge Small Molecules and Polymers for Stable Solar Devices," *Angewandte Chemie International Edition* 61 (2022): 202201844, https://doi.org/10.1002/anie.202201844.

15. F. Qi, Y. Li, R. Zhang, et al., "Dimer Acceptor Adopting a Flexible Linker for Efficient and Durable Organic Solar Cells," *Angewandte Chemie International Edition* 62 (2023): 202303066, https://doi.org/10.1002/anie.202303066.

16. H. Gao, B. Fan, L. Yu, et al., "Correlation of Dimer-Linker-Induced Conformational Lock with Nonradiative Energy Loss in Organic Solar

Cells," *ACS Energy Letters* 9 (2024): 5541–5549, https://doi.org/10.1021/acsenergylett.4c02429.

17. Y. Wang, M. Yang, B. Yin, et al., "An A–D–A′–D–A-Type Narrow Bandgap Electron Acceptor Based on Selenophene-Flanked Diketopyrrolopyrrole for Sensitive Near-Infrared Photodetection," *ACS Applied Materials & Interfaces* 16 (2024): 66846–66856, https://doi.org/10.1021/acsami.3c15365.

18. J. Chen, J. Yang, L. Xiao, et al., "Efficient polymerized small molecular acceptor with selenophene-vinylene-selenophene as a π-bridge for organic solar cells," *Polymer* 334 (2025): 128719, https://doi.org/10.1016/j.polymer.2025.128719.

19. G. Dai, J. Song, J. Deng, et al., "Precise heterodimerization of acceptors for high-efficiency binary organic solar cells," *Matter* 9 (2025): 102465, https://doi.org/10.1016/j.matt.2025.102465.

20. W. Shi, Q. Han, W. Zhao, et al., "A Large Conjugated Rigid Dimer Acceptor Enables 20.19% Efficiency in Organic Solar Cells," *Energy & Environmental Science* 18 (2025): 5356–5364, https://doi.org/10.1039/D5EE00878F.

21. Q. Chen, Q. Wang, S. Meng, et al., "Conjugated Side-Chains Optimize Giant Acceptor Compatibility with Low-Cost Polymer Donor to Overcome the Cost-Efficiency-Stability Trilemma in Polymer Solar Cells," *Advanced Materials* 37 (2025): 2505735, https://doi.org/10.1002/adma.202505735.

22. J. Song, G. Dai, H. Zhang, et al., "Achieving 20.80% Efficiency in Ternary Organic Solar Cells via Suppression of Static and Dynamic Disorder," *Advanced Materials* 38 (2025): 13740, https://doi.org/10.1002/adma.202513740.

23. Y. Bai, T. Chen, X. Ji, et al., "Multi-Selenophene Strategy Enables Dimeric Acceptors-Based Organic Solar Cells with over 18.5% Efficiency," *Advanced Energy Materials* 14 (2024): 2400938, https://doi.org/10.1002/aenm.202400938.

24. W. Feng, Y. Bai, J. Wang, et al., "Rational Design of Two Well-Compatible Dimeric Acceptors Through Regulating Chalcogen-Substituted Conjugated Backbone Enable Ternary Organic Solar Cells with 19.4% Efficiency," *Advanced Energy Materials* 16 (2026): 2404062, https://doi.org/10.1002/aenm.202404062.

25. Z. Jia, S. Qin, L. Meng, et al., "High Performance Tandem Organic Solar Cells via a Strongly Infrared-absorbing Narrow Bandgap Acceptor," *Nature Communications* 12 (2021): 178, https://doi.org/10.1038/s41467-020-20431-6.

26. Z. Zhong, X. Liu, L. Li, et al., "An Asymmetric A-D-π-A Type Non-fullerene Acceptor Enables High-detectivity near-infrared Organic Photodiodes," *Science China Chemistry* 66 (2022): 242–250, https://doi.org/10.1007/s11426-022-1385-8.

27. Q. Fan, H. Fu, M. Liu, et al., "Vinylene-Inserted Asymmetric Polymer Acceptor with Absorption Approaching 1000 Nm for Versatile Applications in all-Polymer Solar Cells and Photomultiplication-Type Polymeric Photodetectors," *ACS Applied Materials & Interfaces* 14 (2022): 26970–26977, https://doi.org/10.1021/acsami.2c02485.

28. Y. Cui, P. Zhu, H. Hu, et al., "Impact of Electrostatic Interaction on Non-Radiative Recombination Energy Losses in Organic Solar Cells Based on Asymmetric Acceptors," *Angewandte Chemie International Edition* 62 (2023): 202304931, https://doi.org/10.1002/anie.202304931.

29. S. Lai, Y. Cui, Z. Chen, et al., "Impact of Electrostatic Interaction on Vertical Morphology and Energy Loss in Efficient Pseudo-Planar Heterojunction Organic Solar Cells," *Advanced Materials* 36 (2024): 2313105, https://doi.org/10.1002/adma.202313105.

30. C. Han, J. Wang, L. Chen, et al., "Balancing Intermolecular Interactions between Acceptors and Donor/Acceptor for Efficient Organic Photovoltaics," *Advanced Functional Materials* 31 (2021): 2107026, https://doi.org/10.1002/adfm.202107026.

31. T. Chen, Y. Zhong, X. Dong, et al., "A p-Type Liquid-Crystal Semiconductor with Synergistic Morphological and Charge-Dynamic Modulation Enables 20.3%-Efficiency Binary Organic Solar Cells," *Advanced Materials* 37 (2025): 12694, https://doi.org/10.1002/adma.202512694.

32. X. Shi, J. W. Qiao, J. Q. Xu, et al., "Non-Contact Dipole Moment Electric Modulation Achieving High Performance near-Infrared Organic Photodetectors," *Advanced Materials* 37 (2025): 10196, https://doi.org/10.1002/adma.202510196.

33. Y. Yang, Y. Sun, D. Gao, et al., "High Performance Near Infrared Organic Photodetectors Realized by Non-Fullerene Acceptors with Reduced Static Energetic Disorder," *Advanced Functional Materials* 36 (2026): 12335, https://doi.org/10.1002/adfm.202512335.

34. M. Liu, W. Li, Z. Peng, et al., "Electron Acceptors Based on Resonant N—B←N Unit with Improved Exciton Dissociation for High-Performance Short-Wavelength Infrared Organic Photodetectors," *Angewandte Chemie International Edition* 64 (2025): e202506116, https://doi.org/10.1002/anie.202506116.

35. H. Hou, W. Wang, T. Li, et al., "Efficient Infrared-Detecting Organic Semiconductors Featuring a Tetraheterocyclic Core with Reduced Ionization Potential," *Angewandte Chemie International Edition* 64 (2025): e202425420, https://doi.org/10.1002/anie.202425420.

36. B. Yin, X. Zhou, Y. Li, et al., "Sensitive Organic Photodetectors with Spectral Response up to 1.3 Mm Using a Quinoidal Molecular Semiconductor," *Advanced Materials* 36 (2024): 2310811, https://doi.org/10.1002/adma.202310811.

37. O. J. Sandberg, C. Kaiser, S. Zeiske, et al., "Mid-gap Trap state-mediated Dark Current in Organic Photodiodes," *Nature Photonics* 17 (2023): 368–374, https://doi.org/10.1038/s41566-023-01173-5.

38. X. Chen, Y. Zhu, Y. Xu, et al., "Design of Ultra-Narrow Bandgap Polymer Acceptors for High-Sensitivity Flexible All-Polymer Short-Wavelength Infrared Photodetectors," *Angewandte Chemie International Edition* 64 (2024): 202413965, https://doi.org/10.1002/anie.202413965.

39. Y. Zhu, H. Chen, R. Han, et al., "High-speed Flexible near-infrared Organic Photodiode for Optical Communication," *National Science Review* 11 (2024): nwad311, https://doi.org/10.1093/nsr/nwad311.

40. J. Liu, X. Wu, X. Liu, E. Li, Z. Jiao, and S. Yin, "UV-A/B High-Sensitivity Organic Photodetectors Containing Butterfly-Shaped Furan-Fused BN-Dihydropyrene with Push-Pull Electron "Wings" toward Image Sensor," *Advanced Functional Materials* 34 (2024): 2404870, https://doi.org/10.1002/adfm.202404870.

41. J. Zeng, Z. Ren, D. Lin, et al., "Molecular-Device Co-Engineering of Ultra-Low Dark Current SWIR Organic Photodetectors for High-Quality Blood-Pressure Monitoring and Optical Communication," *Advanced Materials* 37 (2025): 09923, https://doi.org/10.1002/adma.202509923.

42. W. Chen, Y. Zhang, X. Zhu, J. Miao, J. Liu, and L. Wang, "Near-infrared Organic Photodetectors Outperform Si Photodetectors: Introducing an All-fused-ring Acceptor into Active Layers for Ultra-low Trap Density," *Science China Materials* 68 (2025): 1359–1368, https://doi.org/10.1007/s40843-024-3251-x.

43. X. Zhu, C. Gu, Y. Cheng, et al., "3D-Architectured Acceptor with High Photoluminescence Quantum Yield and Moderate Crystallinity for High-Efficiency Organic Solar Cells with Low Voltage Loss," *Advanced Materials* 37 (2025): 2507529, https://doi.org/10.1002/adma.202507529.

44. Z. Zhong, S. Gámez-Valenzuela, J.-W. Lee, et al., "Three-dimensional Bowl-shaped Solid Additive Achieves 20.52% Efficiency Organic Solar Cells with Enhanced Thermal Stability via Curvature-mediated Morphology Regulation," *Energy & Environmental Science* 18 (2025): 7635–7647, https://doi.org/10.1039/D5EE01977J.

45. W. Feng, T. Chen, Y. Li, et al., "Binary All-Polymer Solar Cells with a Perhalogenated-Thiophene-Based Solid Additive Surpass 18 % Efficiency," *Angewandte Chemie International Edition* 63 (2024): 202316698, https://doi.org/10.1002/anie.202316698.

46. J. Wang, Z. Zhang, Y. Wang, et al., "A chlorinated Thiophene Flexible-bridged Dimeric Acceptor for Stable Organic Solar Cells with 19.6% Efficiency," *EES Solar* 1 (2025): 819, https://doi.org/10.1039/D5EL00090D.

47. C. Gao, Y. Wang, H. Tian, et al., "Prolonged-Nucleation Strategy via an Asymmetric Brominated Acceptor Enables >20% Efficiency in Five Different Organic Solar Cells," *Advanced Materials* 38 (2025): 17576, https://doi.org/10.1002/adma.202517576.

48. Y. Zhang, Y. Yu, X. Liu, et al., "An n-Type All-Fused-Ring Molecule with Photoresponse to 1000 Nm for Highly Sensitive Near-Infrared Photodetector," *Advanced Materials* 35 (2023): 2211714, https://doi.org/10.1002/adma.202211714.

49. Z. Wei, Y. Wang, Y. Li, et al., "High-efficiency, Ultra-flexible Organic Solar Cells Enabled by Chloroprene Rubber as both a Non-volatile Solid Additive and Plasticizer," *Joule* 9 (2025): 101996, https://doi.org/10.1016/j.joule.2025.101996.

50. J. Ma, J. Wang, Z. Peng, J. Hu, J. Liu, and Y. Liu, "Highly Transparent Organic Photodetectors with Transfer-printed PEDOT:PSS Top Electrodes," *Science China Materials* 68 (2025): 4051–4058, https://doi.org/10.1007/s40843-025-3518-2.

51. J. Wang, K. Yao, K. Cui, et al., "Contact Electrification Induced Multicolor Self-Recoverable Mechanoluminescent Elastomer for Wearable Smart Light-Emitting Devices," *Advanced Optical Materials* 11 (2023): 2203112, https://doi.org/10.1002/adom.202203112.

52. H. Ding, J. Q. Lu, K. M. Jacobs, and X.-H. Hu, "Determination of Refractive Indices of Porcine Skin Tissues and Intralipid at Eight Wavelengths between 325 and 1557 Nm," *Journal of the Optical Society of America A* 22 (2005): 1151, https://doi.org/10.1364/JOSAA.22.001151.

53. W. Li, P. Xiong, X. Zheng, et al., "Micro-Strain Responsive Near-Infrared Mechanoluminescence for Potential Nondestructive Artificial Joint Stress Imaging," *Advanced Materials* 38 (2025): 05360, https://doi.org/10.1002/adma.202505360.

Supporting Information

Additional supporting information can be found online in the Supporting Information section.

Supporting File: smll72839-sup-0001-SuppMat.docx.